Quantum Electronics **47** (6) 553–560 (2017)

OPTICAL FIBRES

https://doi.org/10.1070/QEL16332

Multiband supercontinuum generation in an air-core revolver fibre

Yu.P. Yatsenko, E.N. Pleteneva, A.G. Okhrimchuk, A.V. Gladyshev, A.F. Kosolapov, A.N. Kolyadin, I.A. Bufetov

Abstract. **Multiband supercontinuum generation in an air-core revolver fibre having a large number of transmission bands in a wide spectral range has been studied experimentally and theoretically for the first time. The fibre fabricated by us possesses unique dispersion and guidance characteristics for radiation transfer from one band to another despite the high losses at the band boundaries. In our experiments, launching 205-fs laser pulses of 110 μJ energy at 1028 nm into the fibre we have obtained a supercontinuum spanning the spectral range from 415 to 1593 nm, with 11 transmission bands. Numerical simulation suggests that, in the case of single-mode propagation of pulses with such energy in the fibre, the supercontinuum may span 14 transmission bands and have a spectral width above three octaves, with a long-wavelength edge at 4200 nm.**

Keywords: *hollow-core microstructured fibres, femtosecond pulses, supercontinuum.*

1. Introduction

Hollow-core microstructured fibres (HCMFs) offer wide possibilities for transmitting high-power laser light. Owing to the high degree of light localisation in their core, the light propagates in the gaseous medium that fills the core and has low dispersion and nonlinearity. Because of this, such fibres enable transmission of ultrashort pulses with energies of up to several hundred microjoules without significant distortion [1–3]. Moreover, one important advantage of the HCMFs is the possibility of controlling the nonlinear properties of the active medium by filling the fibre with various gases under pressure [4]. Gaseous media have very high optical breakdown thresholds for ultrashort pulses, so, even at small nonlinear coefficients, high-power light is capable of causing various nonlinear processes, including supercontinuum generation, at sufficiently long fibre lengths.

Impressive advances in UV supercontinuum generation by femtosecond pulses were made using hydrogen-filled hollow-core fibres with a Kagome lattice cladding [4, 5]. Controlling fibre dispersion and guidance characteristics by varying the gas pressure, Belli et al. [5] obtained a record low value (124 nm) for the short-wavelength edge of the supercontinuum, with the supercontinuum spectrum spanning more than three octaves: from 124 to 1200 nm. In addition, such fibres enabled the generation of a supercontinuum in the form of a Raman comb (a sequence of broadened Stokes and anti-Stokes spectral components of Raman scattering in hydrogen) extending from the UV to the mid-IR [6–9]. The Kagome cladding fibre used for supercontinuum generation in the studies in question had one or a few broad transmission bands, which limited the spectral width of the supercontinuum.

In hollow-core revolver fibres (HCRFs) with a cladding formed by a single ring of standard capillaries or a few rings of nested capillaries [10–16], the light confinement mechanism is determined by the negative curvature of the reflective cladding [17, 18]. Unlike Kagome lattice fibres, which have broad transmission bands, an HCRF may have a large number of narrower bands, with low losses in their centre. Their boundaries can be found approximately from the resonance condition for a planar interferometer in the ARROW model [19]:

$$\lambda_m = \left(\frac{2n_1 d}{m}\right)\left[\left(\frac{n_2}{n_1}\right)^2 - 1\right]^{1/2}, \quad m = 1, 2, ...,$$

where λ_m is the wavelength corresponding to the transmission minimum in the mth band; d is the capillary wall thickness; n_1 is the refractive index of the gaseous medium filling the core; and n_2 is that of the cladding material. It follows from this condition that, in the case of a weakly dispersive gaseous medium, the transmission bands have almost identical spectral widths.

The high degree of light localisation in HCRFs makes it possible to obtain lower losses in the centre of each band and shift the long-wavelength edge of the supercontinuum farther into the mid-IR region in comparison with Kagome cladding fibres. To the best of our knowledge, a supercontinuum spanning a large number of transmission bands in a hollow-core fibre has not been previously investigated.

This paper presents an experimental and theoretical study of the feasibility of obtaining a multiband supercontinuum in an HCRF with a cladding formed by noncontacting single-wall capillaries. Launching 205-fs laser pulses of 110 μJ energy at 1028 nm into a fibre filled with atmospheric air, we experimentally obtain a supercontinuum spanning the spectral range from 415 to 1593 nm, with 11 transmission bands. We examine the basic nonlinear processes responsible for the

Yu.P. Yatsenko, A.V. Gladyshev, A.F. Kosolapov, A.N. Kolyadin, I.A. Bufetov Fiber Optics Research Center, Russian Academy of Sciences, ul. Vavilova 38, 119991 Moscow, Russia;
e-mail: yuriya@fo.gpi.ru;
E.N. Pleteneva Moscow Institute of Physics and Technology (State University), Institutskii per. 9, 141701 Dolgoprudnyi, Moscow region, Russia;
A.G. Okhrimchuk International Center of Laser Technology, Dmitry Mendeleev University of Chemical Technology, Miusskaya pl. 9, 125047 Moscow, Russia

Received 28 February 2017; revision received 18 April 2017
Kvantovaya Elektronika **47** (6) 553–560 (2017)
Translated by O.M. Tsarev

pulse energy distribution over the transmission bands. Numerical analysis indicates that, in the case of the above input pulse parameters and single-mode pulse propagation in the fibre, the long-wavelength edge of the supercontinuum can be shifted to 4200 nm, spanning 14 transmission bands of the fibre.

2. Fibre characteristics

To study the supercontinuum, we fabricated a fibre whose cross section is shown in Fig. 1. The reflective cladding of the hollow-core fibre consists of eight noncontacting capillaries symmetrically arranged around a 61.5-μm-diameter core. The wall thickness of the capillaries is 2.7 μm and their outer diameter is 25 μm.

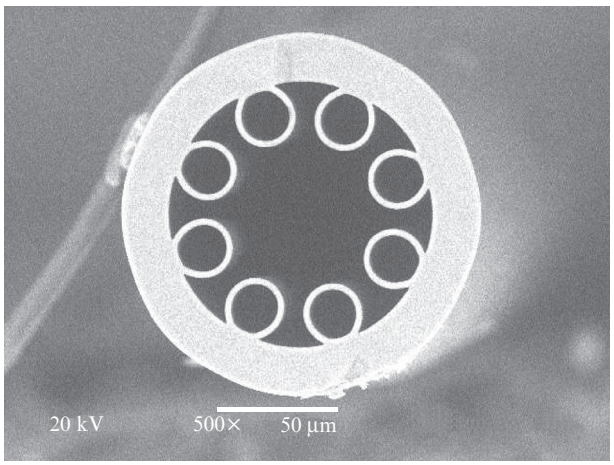

Figure 1. Cross-sectional electron micrograph of the hollow-core optical fibre.

Guidance and dispersion characteristics in 14 transmission bands of the fibre, which span the wavelength range from 370 nm to 5 μm, were calculated by the finite element method using standard COMSOL software. Figure 2a shows calculated fundamental mode loss in the wavelength range corresponding to the 14 transmission bands. According to the mechanism in the ARROW model, all the transmission bands of the fibre have almost identical widths (54 ± 5 THz), but the negative curvature of the core–cladding boundary shifts the edges of the bands to shorter wavelengths (within 5%) in comparison with the above resonance condition for a planar interferometer. Figure 2b shows spectral losses calculated for the six lower order modes in the fourth to sixth transmission bands. Also shown are the losses measured in these bands [curves (I)–(III)]. It is seen that the measured fundamental mode loss is two or more orders of magnitude higher than the calculated one and that the difference increases with increasing band number (and decreasing wavelength). This can be accounted for by the fact that the measured loss corresponds to the loss of the higher order modes and their number increases with decreasing wavelength (increasing band number). It follows from Fig. 2b that, in the fifth band, which includes the emission wavelength (1028 nm) of the laser used, the calculated loss of four modes (LP_{01}, LP_{11}, LP_{21} and LP_{02}) is lower than the measured one. The calculated 0.1 dB m^{-1} width of the fifth band for the fundamental mode is 148 nm. The mode field diameter at a wavelength of

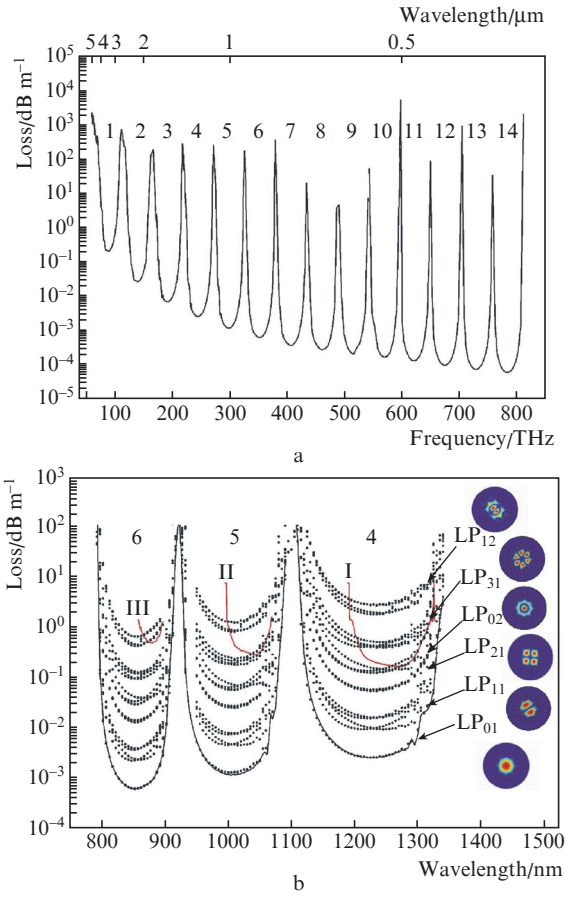

Figure 2. (Colour online) (a) Calculated fundamental mode loss in the spectral range corresponding to 14 transmission bands; (b) experimentally measured loss [curves (I)–(III)] and calculated loss (dotted curves) for the six lower order modes with different polarisation directions in the fourth to sixth transmission bands (the fundamental mode LP_{01} loss is shown by solid lines).

1028 nm is 45 μm and the calculated fundamental mode loss is 1.32×10^{-3} dB m^{-1}.

Figure 3 shows the spectral dependence of the second-order dispersion coefficient in the fourth to sixth bands for the fundamental mode (LP_{01}) and one of the lower order modes (LP_{21}). In the central part of each band, the dispersion

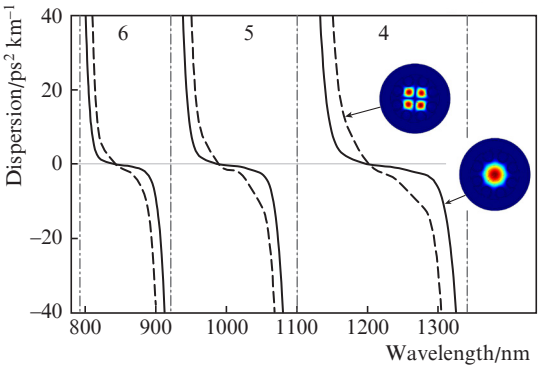

Figure 3. (Colour online) Spectral dependence of second-order dispersion in the fourth to sixth bands for the LP_{01} and LP_{21} modes. The dot-dashed lines show the boundaries of the transmission bands.

of each mode has one zero. It can be seen that the dispersion curves of the two modes have almost identical zero-dispersion wavelengths and differ only in slope.

The zero-dispersion wavelengths for the fundamental mode in the three bands are $\lambda_{04} = 843$ nm, $\lambda_{05} = 989$ nm and $\lambda_{06} = 1201$ nm. At a wavelength $\lambda = 1028$ nm, the dispersion of the fundamental mode is $\beta_2 = -1.16$ ps^2 km^{-1}. Similar dispersion curves were obtained for the other bands.

3. Experimental

The beam of a PHAROS-SP femtosecond laser generating 205-fs pulses at a wavelength of 1028 nm with a repetition rate of 1 kHz was focused by a plano-convex lens ($f = 10$ cm) onto the end face of a 3-m-long segment of the fibre. The lens with this focal length allowed us to optimise light launch conditions. The beam waist diameter at the input fibre end was 42 μm. The femtosecond pulse energy was varied using a polarising attenuator. The maximum pulse energy at the HCRF input was 130 μJ.

Figure 4a shows intensity distributions at the fibre output at an input pulse energy of ~100 nJ and varied light launch conditions. It is seen that at least four lower order modes can simultaneously propagate in the 3-m-long fibre. Figure 4b illustrates the effect of an increase in pulse energy from 7 to 130 μJ on the mode field distribution at the fibre output under given light launch conditions. The mode symmetry is seen to be markedly distorted, which is attributable to the presence of higher order modes due to energy transfer from the fundamental mode through nonlinear processes [20].

Figure 5 shows the measured fibre transmittance as a function of input pulse energy. The rapid, almost linear decrease in transmittance from 75% to 40% in the initial portion of the curve, at pulse energies below 30 μJ, gives way to a slower decrease at higher energies. One possible reason for the rapid drop in the initial portion of the curve is radiation transfer to higher order modes, which have higher losses, through nonlinear effects.

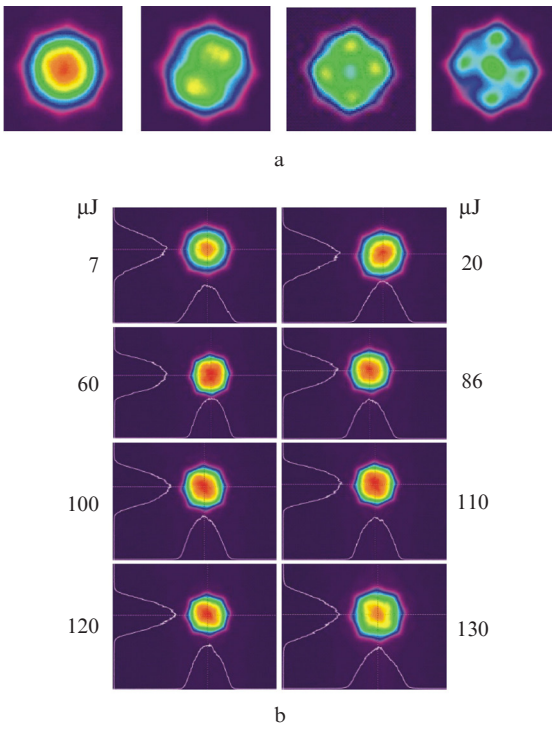

Figure 4. (Colour online) Effects of (a) light launch conditions and (b) input pulse energy (7, 20, 60, 86, 100, 110, 120 and 130 μJ, respectively) on the intensity distribution obtained at the fibre output using a Spiricon camera.

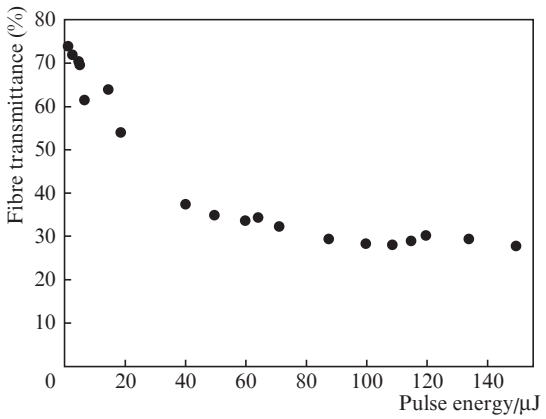

Figure 5. Fibre transmittance as a function of input pulse energy.

Figure 6 shows fibre output spectra obtained at input pulse energies in the ranges 2.5 nJ to 3 μJ (Fig. 6a) and 5 to 24 μJ (Fig. 6b). The spectra were measured in the wavelength range 1000–1100 nm, corresponding to the fifth transmission

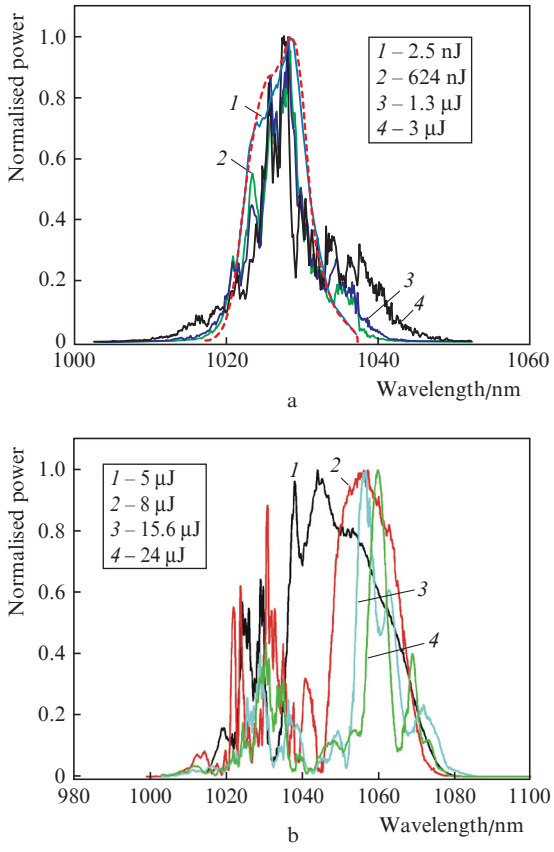

Figure 6. (Colour online) Laser emission spectrum measured at the output of the 3-m-long fibre at input pulse energies (a) from 2.5 nJ to 3 μJ and (b) from 5 to 24 μJ. The dashed line in Fig. 6a shows the spectrum of the laser pulses at the fibre input.

band of the fibre, which includes the input pulse wavelength: 1028 nm. It follows from Fig. 6a that the spectrum obtained at an input pulse energy of 2.5 nJ is similar in shape to the spectrum of the input pulse, whereas at an energy of 624 nJ the shape of the spectrum is distorted by modulation, which increases with increasing pulse energy. The distortion of the spectrum may be caused by Kerr nonlinearity, rotational stimulated Raman scattering (SRS) and intermode coupling. It is worth noting that, in the pulse energy range under consideration, we observe no SRS-induced shift of the spectral maximum. The effect of SRS shows up only as marked asymmetry of the wings at an energy of 3 μJ. A considerable shift of the spectral maximum to longer wavelengths is observed in Fig. 6b. As the energy is raised to 24 μJ, the shift reaches 32 nm and the full width at half maximum of the spectrum decreases by a factor of 1.8.

The measured spectra of input pulses having energies from 80 to 130 μJ demonstrate spectral broadening considerably exceeding the width of the fifth transmission band, which corresponds to the input pulse wavelength. Figure 7 shows one such spectrum, measured at an input pulse energy of 110 μJ. The spectrum has the form of a supercontinuum extending from 415 to 1593 nm and spanning 11 transmission bands. The observed output emission of the fibre is shown in Fig. 8.

A characteristic feature of the supercontinuum thus obtained is that it has a band structure, with dips in the spectrum at wavelengths corresponding to the peak loss region at the boundary between the transmission bands. The width of the spectral dips varies from tens to hundreds of nanometres, depending on the pulse energy and the number of the transmission band.

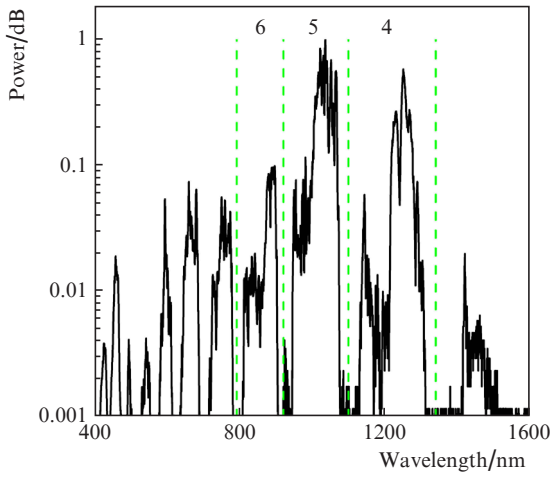

Figure 7. Laser emission spectrum measured at the output of the 3-m-long fibre at an input pulse energy of 110 μJ.

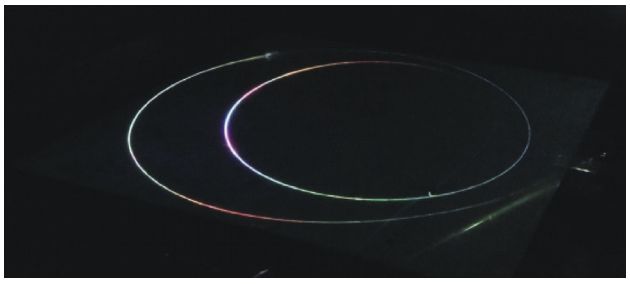

Figure 8. (Colour online) Emission from the fibre at an input pulse energy of 130 μJ.

4. Numerical analysis results and comparison with experimental data

The technique used to simulate pulse propagation in a hollow-core fibre was similar to that described previously [15]. Numerical simulation was performed for transform-limited Gaussian pulses propagating in a single-mode fibre filled with atmospheric air at a pressure of 1 atm. The pulse parameters at the fibre input corresponded to experimentally determined values. In numerical analysis of femtosecond pulse propagation in an HCRF, we used a generalised nonlinear Schrödinger equation for a complex-valued spectral pulse envelope [21], which takes into account higher order dispersion, Kerr nonlinearity and SRS by rotational transitions of nitrogen. We assumed that, in the case of 200-fs pulses, the Kerr effect and SRS made equal contributions to the nonlinear refractive index: $n_{2K} = n_{2R} = 3 \times 10^{-23}$ m^2 W^{-1} [22–25]. The Raman response function of atmospheric nitrogen, $h_R(t)$, was represented in the form [23]

$$h_R(t) = \Omega^2 \tau_s \exp\left(-\frac{t}{\tau_d}\right)\sin\left(\frac{t}{\tau_s}\right),$$

where $\Omega^2 = \tau_s^{-2} + \tau_d^{-2}$; $\tau_s = 1/\omega_R$; ω_R is the cyclic frequency of the transition between the $J = 8$ and $J = 6$ rotational levels of the N_2 molecule ($\omega_R = 1.6 \times 10^{13}$ s^{-1}); $\tau_d = 1/\Gamma_2$; and $\Gamma_2 = 1.3 \times 10^{13}$ s^{-1} is the dephasing rate of the dipole moment of the $J = 8$ excited rotational state.

Numerical analysis was carried out in the Matlab environment using built-in algorithms for performing the fast Fourier transform and solving the equation by the fourth-order Runge–Kutta method. The spectral range containing 14 transmission bands (from 370 nm to 5 μm) was divided into 2^{15} intervals. The maximum time interval was then 40 ps. The spectral dependences of the loss and effective refractive index for a particular mode were calculated with COMSOL Multiphysics.

Figure 9 shows the calculated pulse spectrum and shape at the output of a 3-m-long air-filled fibre for a transform-limited Gaussian pulse at an input pulse energy of 6 μJ. The calculation results are presented for the LP_{01} (Figs 9a, 9b) and LP_{21} modes (Figs 9c, 9d) under the assumption that only one of these modes, with an energy of 6 μJ, propagates through the fibre. Pulses in these modes differ only slightly in spectrum and shape: a pulse propagating in the fundamental mode, which has lower dispersion, has a more severe nonlinear distortion of its spectrum and a shorter time delay. Comparison of the spectra in Fig. 9 with the measured spectra in the power range under consideration (Fig. 6) demonstrates more significant distinctions.

The measured spectra have an additional, random modulation. At the same time, their peaks are markedly less shifted from the input pulse wavelength. The most likely cause of the random modulation is intermode coupling. The software used in our simulations leaves it out of account, but it allows us to find from the Stokes shift of the spectral maximum that the energy in the fibre is not fully localised in the fundamental mode. For example, the calculated shift of the spectral maximum at a fibre length of 3 m and pulse energy of 6 μJ is 34 nm

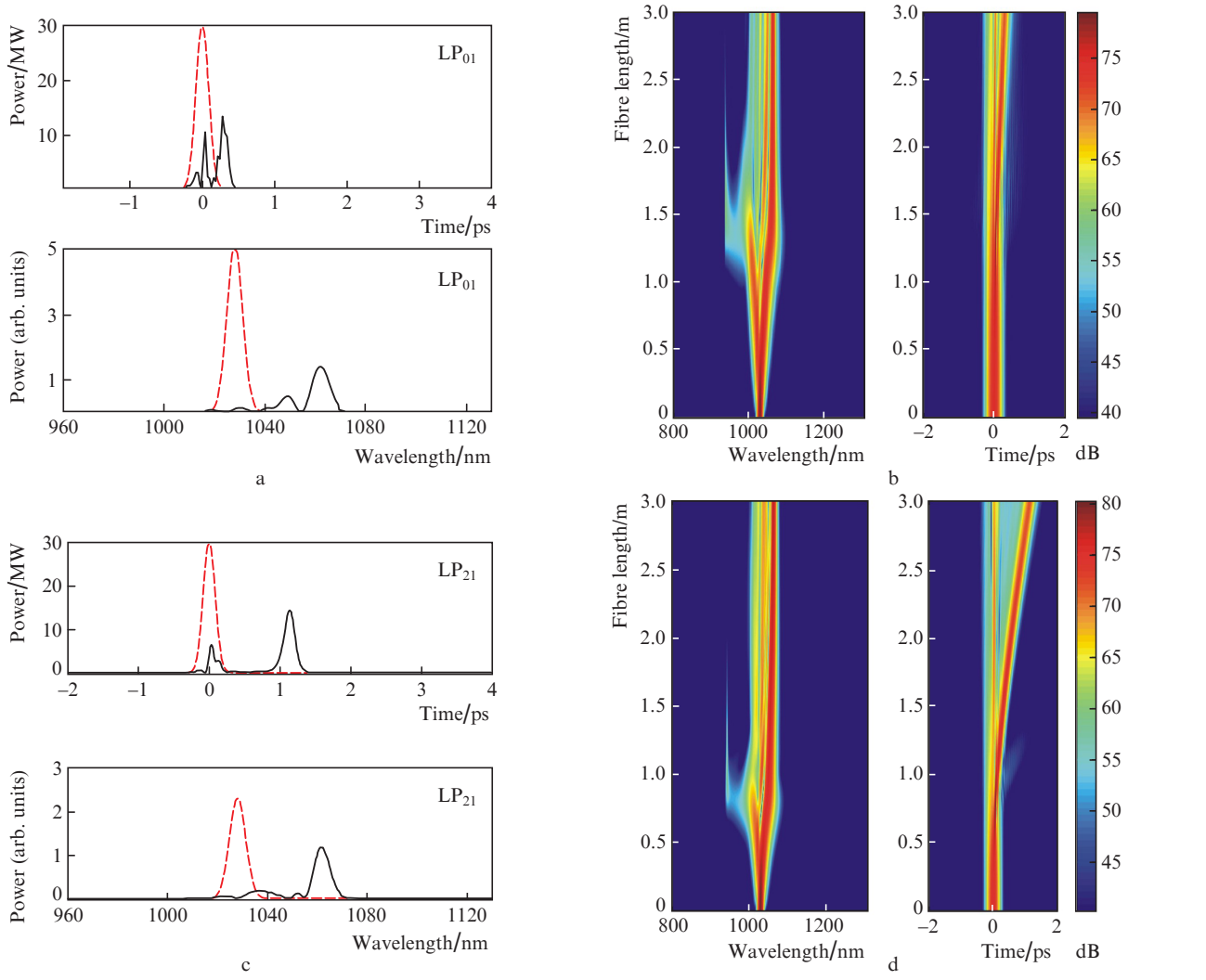

Figure 9. (Colour online) Propagation of a transform-limited 200-fs Gaussian pulse in the LP_{01} and LP_{21} modes at an input pulse energy of 6 μJ in each mode: pulse shape and spectrum at the output of the 3-m-long fibre for the (a) LP_{01} and (c) LP_{21} modes; rainbow colour maps illustrating the evolution of the pulse spectrum and shape along the length of the fibre for the (b) LP_{01} and (d) LP_{21} modes. Here and in Fig. 10, dashed lines represent the pulse shape and spectrum at the fibre input.

for both modes. In the measured spectrum, roughly the same shift (32 nm) was obtained at an input energy of 24 μJ. Since the Stokes shift scales linearly with power, this gives grounds to believe that the input energy redistributes in the fibre between different modes that have lower peak power in comparison with the peak power in the case of single-mode propagation.

The rainbow colour maps presented in Fig. 9 demonstrate characteristic features of the propagation of a pulse whose spectrum lies within one transmission band. It is seen that the pulse spectrum and shape vary significantly along the length of the fibre. Over the first metre of the fibre, the main effect is produced by self-phase modulation. As a result, the spectrum broadens and the pulse shape remains almost unchanged. At fibre lengths above 1 m, effects such as pulse self-steepening and Raman self-frequency shift cause the pulse to break up into Raman solitons propagating at various velocities, thus leading to a shift of the spectral maximum towards the long-wavelength edge of the band and dispersive wave generation at its short-wavelength edge. In the rainbow colour maps, one can see the formation of a 936-nm dispersive wave when the maximum in the spectrum of a Raman soliton shifts by 30 nm towards the long-wavelength edge of the band. Upon a further shift of the soliton, the spectrum of the dispersive wave shifts to the strong absorption region at the short-wavelength edge of the band (in accordance with the phase-matching condition) and the wave decays over a distance of ~1 m. At a pulse energy of 6 μJ, no radiation transfer to neighbouring bands is detectable up to a power level of –40 dB. At the same time, at 12 μJ there is energy transfer to neighbouring bands, which leads to supercontinuum generation (Fig. 10).

Figure 11 shows supercontinuum spectra calculated for different fibre lengths at a pulse energy of 110 μJ in one mode. The maximum supercontinuum width (370–2760 nm at the –30 dB power level and 370–4200 nm at the –50 dB level) is reached at a length as short as 50 cm. Over the first 50 cm of the fibre, losses have a weak effect on the efficient nonlinear processes. The spectrum has a relatively smooth shape, with a reduced depth and width of the dips at the boundaries of the bands. At a fibre length of 1.5 m, the spectrum assumes a well-defined band structure. Further pulse propagation, up to the fibre output, has little or no effect on the shape of the spectrum, except that the dips at the edges of the absorption bands become sharper.

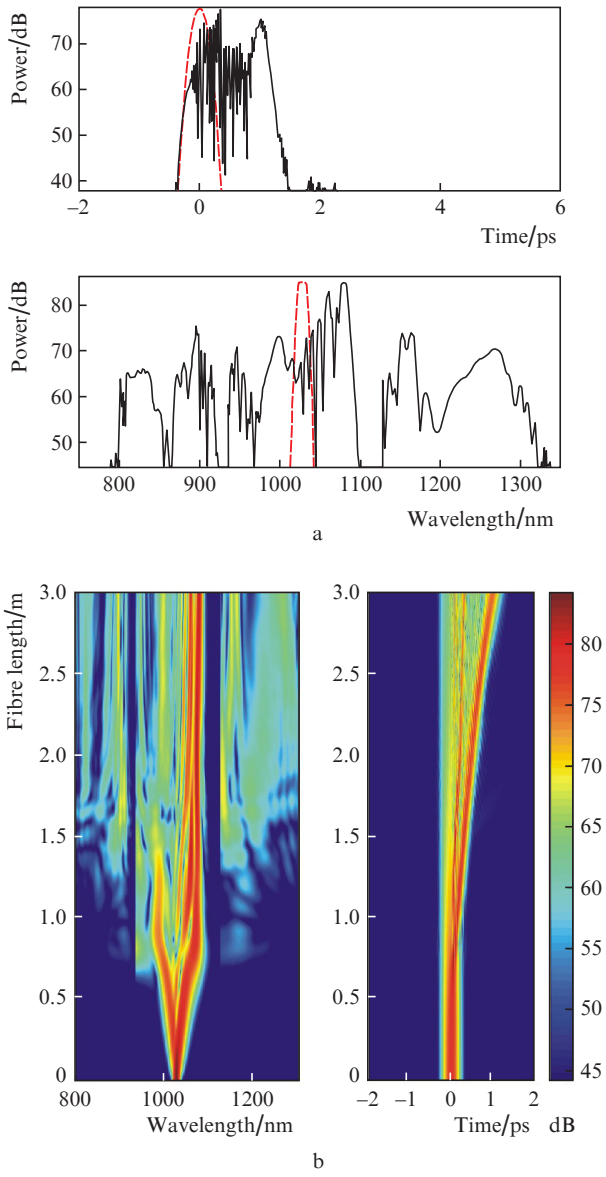

Figure 10. (Colour online) Propagation of a transform-limited 200-fs Gaussian pulse in the LP_{01} mode at an input pulse energy of 12 μJ: (a) pulse shape and spectrum at the output of the 3-m-long fibre; (b) rainbow colour maps illustrating the evolution of the pulse spectrum and shape along the length of the fibre.

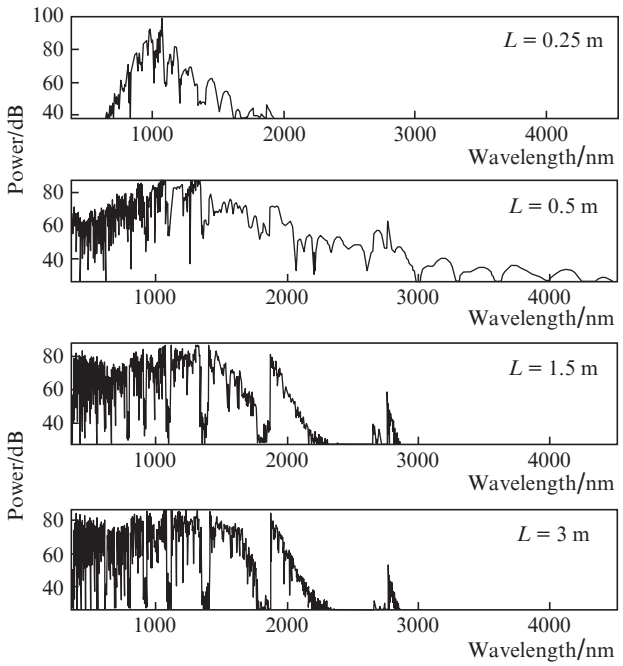

Figure 11. Calculated supercontinuum spectra at different fibre lengths for the LP_{01} mode at an input pulse energy of 110 μJ.

Figure 12a demonstrates how the energy of a 200-fs pulse with an input energy of 110 μJ varies in the course of pulse propagation through the fibre. At a length of 50 cm, where the spectrum has the maximum width, the pulse retains 55% of its input energy. Figure 12b shows a theoretical dependence of the width of the supercontinuum spectrum on pulse energy in one fibre mode. The width of the supercontinuum spectrum is comparable to the experimentally determined one at far lower input pulse energies. This can be accounted for by the considerable decrease in the peak pulse power in the fibre because of the energy redistribution over several modes.

The main mechanisms responsible for energy transfer to neighbouring bands are modulation instability due to four-photon nonlinear processes (degenerate and nondegenerate four-wave mixing) and the generation of dispersive waves. This is illustrated in Fig. 13, where arrows mark peaks related to each other by nonlinear processes in the fourth to sixth transmission bands of the measured spectrum (Fig. 7) at an input pulse energy of 110 μJ and peak power P_{in} = 550 MW. In particular, the wavelengths 1251, 1036 and 884 nm of the S(P1), P1 and AS(P1) peaks, located in the fourth, fifth and sixth transmission bands, respectively, satisfy the condition of a degenerate four-wave process ($2\omega_{1036} = \omega_{1251} + \omega_{884}$). In this process, light at the wavelength of the P1 peak in the fifth band serves to pump the Stokes component at the wavelength of the S(P1) peak in the fourth band and the anti-Stokes component at the wavelength of the AS(P1) peak in the sixth band. The above condition is also met by the S(P3), P3 and AS(P3) peaks, located at wavelengths of 1230, 1030 and 886 nm ($2\omega_{1030} = \omega_{1230} + \omega_{886}$), and the S(P4), P4 and AS(P4) peaks, located at 1290, 1052 and 889 nm ($2\omega_{1052} = \omega_{1290} + \omega_{889}$). Two peaks in the fifth band, P1 (1036 nm) and P2 (1022 nm), are related to the S(P3) (1230 nm) and AS(P1) (884 nm) peaks in the fourth and sixth bands, respectively, by a condition corresponding to a nondegenerate four-wave process: $\omega_{1036} + \omega_{1022} = \omega_{1230} + \omega_{884}$. In addition, a nondegenerate four-wave process determines the energy redistribution between the P1 (1036 nm) and P4 (1052 nm) peaks in the fifth band and the S(P1, P4) and AS(P1, P4) peaks at wavelengths of 1268 and 887 nm, respectively, in the fourth and sixth bands ($\omega_{1036} + \omega_{1052} = \omega_{1268} + \omega_{887}$).

The presence of peaks related by nonlinear processes and located in different transmission bands at the output of the 3-m-long fibre suggests high efficiency of four-photon processes for widely separated pump, signal and idler wavelengths. This can be accounted for primarily by the very high degree of light localisation in air, a weakly dispersive medium. As a result, the effective refractive indices of each mode differ little even at a large separation between the bands. Moreover, an important role in ensuring phase matching and efficient energy transfer from one band to another is played by the presence of a zero second-order dispersion point in the centre of each band. For example, calculations for the fundamental mode indicate that the phase matching condition $\Delta\beta = 2\beta_{1036} -$

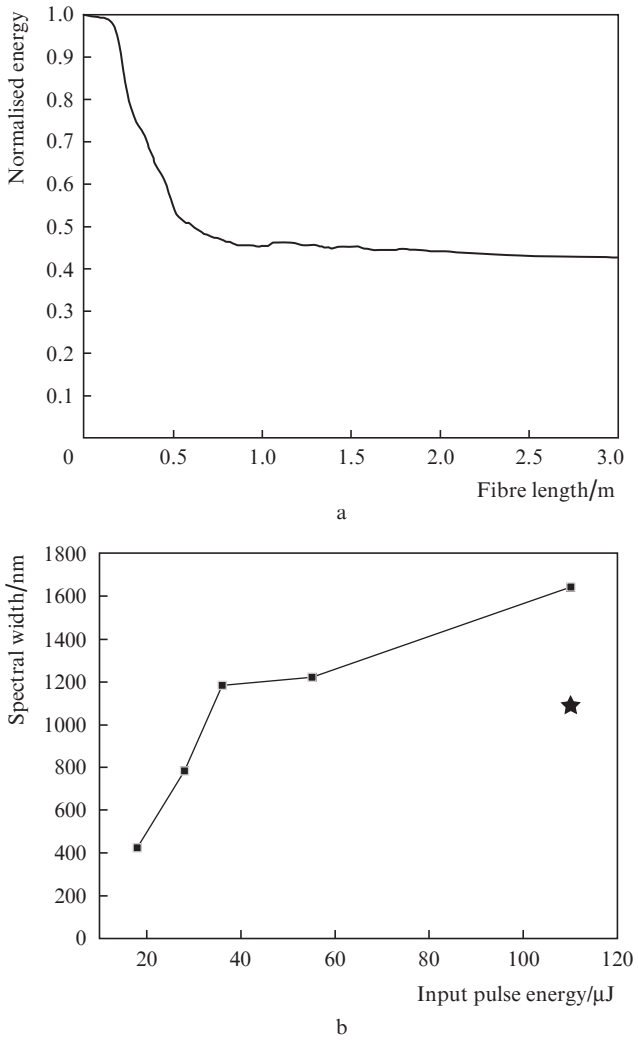

Figure 12. (a) Pulse energy as a function of fibre length for a 200-fs pulse with an input energy of 110 μJ propagating through the fibre; (b) –30 dB width as a function of input pulse energy for the supercontinuum spectrum at the output of the 3-m-long fibre at a pulse duration of 200 fs (the filled squares represent calculation results and the asterisk represents the value determined experimentally at a pulse energy of 110 μJ).

$\beta_{1251} - \beta_{884} + 2\gamma P = 0$ (where β is the propagation constant; γ is the nonlinearity coefficient; and P is the pump power) for the $2\omega_{1036} = \omega_{1251} + \omega_{884}$ process is satisfied exactly at a pump power $P_{1036} = 58$ MW. The wavelengths involved in this process lie in the negative dispersion region at roughly the same distance from the zero dispersion point in their bands and are similar in second-order dispersion (β_2 is –1.439, –1.314 and –1.89 ps^2 km^{-1} at wavelengths of 1036, 1251 and 884 nm, respectively). Given that the transmission bands of the fibre differ little in spectral width, the Stokes and anti-Stokes lines in the fourth and sixth bands can be used as pump sources for efficient radiation transfer near the zero dispersion point to the third and seventh bands, respectively. At a sufficient power of femtosecond pulses, such a cascade process may involve a large number of transmission bands and lead to broadband supercontinuum generation, despite the losses at the band edges.

Energy transfer to neighbouring bands may also be due to dispersive wave generation. Figure 13 shows a peak in the fourth band at a wavelength $\lambda_D = 1144$ nm, which satisfies the

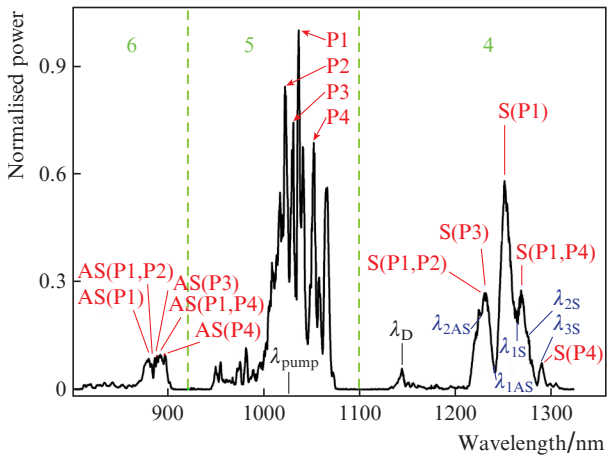

Figure 13. (Colour online) Nonlinear processes determining energy transfer between three neighbouring transmission bands in the spectrum measured at an input pulse energy of 110 μJ. The portion of the spectrum corresponding to the fourth to sixth transmission bands in Fig. 7 is shown on a linear scale. See text for notation.

phase matching condition for a dispersive wave, $\Delta\beta_D = \beta(\omega_S) - \beta(\omega_D) - \beta_1(\omega_S - \omega_D) + 0.5\gamma P = 0$ (where ω_S and ω_D are the soliton and dispersive wave cyclic frequencies, respectively, and $\beta_1 = (d\beta/d\omega)_{\omega_S}$), during the propagation of a soliton with a power $P = 276$ MW at a wavelength $\lambda_S = 1028$ nm in the fifth band.

For efficient energy transfer from one band to another, the Stokes shift of rotational SRS in atmospheric nitrogen is too small (75 cm^{-1}), but within each band it plays an active role in spectrum broadening. Figure 13 specifies the wavelengths corresponding to energy transfer in the fourth band from shorter to longer wavelength components due to rotational SRS. The structure of the major peak at 1251 nm is modulated at a frequency of 75 cm^{-1}, with dips in the shorter wavelength region and peaks in the longer wavelength region.

5. Conclusions

The fibre described in this report possesses unique dispersion and guidance characteristics for supercontinuum generation. It follows from the present numerical simulation results that the cladding parameters used in its design make it possible to obtain UV to mid-IR transmission bands essentially identical in spectral width and shape. Owing to the low dispersion of air, the dispersion characteristics of a particular mode in transmission bands identical in shape are also essentially identical. The presence of zero second-order dispersion points near the centre of each band ensures favourable conditions for efficient energy transfer from one band to another due to nonlinear effects.

In our experiments, launching 205-fs pulses of 110 μJ energy into the fibre, we have obtained a supercontinuum spanning the wavelength range from 415 to 1593 nm, with 11 transmission bands. Multimode light propagation in the HCRF studied here reduces the efficiency of the nonlinear processes responsible for supercontinuum generation because of the energy redistribution between the modes. The present numerical simulation results indicate that, in the case of pulse powers near those in our experiments and single-mode operation of the HCRF, the supercontinuum may span 14 transmission bands, extending from 370 to 4200 nm. Such spectral

width (over three octaves) can be obtained at a fibre length of ~50 cm. The pulse then retains more than 50% of its energy.

Examining the structure of the spectrum in different transmission bands, we have identified the main nonlinear processes responsible for energy transfer from one band to another, such as degenerate and nondegenerate four-wave mixing and the generation of dispersive waves by solitons. It is worth emphasising the high efficiency of nonlinear cascade processes in an HCRF filled with atmospheric air owing to the uniform distribution of zero dispersion points over a wide spectral region.

Rotational SRS in nitrogen has a negative effect on multiband supercontinuum generation. Even though its Stokes and anti-Stokes components contribute to rapid broadening of the spectrum within each band, the Stokes shift is too small for radiation transfer from one band to another. Moreover, the Raman shift of the spectral maximum within each band leads to a shift of the energy in the spectrum towards the long-wavelength edges of the transmission bands, where it is rapidly absorbed. The SRS-induced radiation losses at the boundaries between the transmission bands can be avoided by filling the fibre core with gaseous media such as argon, in which no such effect occurs.

It follows from the present results that optimising the HCRF design for achieving single-mode propagation will make it possible to extend the multiband supercontinuum to both the UV and mid-IR.

Acknowledgements. This work was supported by the Russian Science Foundation (Grant No. 16-19-10513).

References

1. Wang Y.Y., Peng X., Alharbi M., Dutin C.F., Bradley T.D., Gérôme F., Mielke M., Booth T., Benabid F. *Opt. Lett.*, **37**, 3111 (2012).
2. Debord B., Alharbi M., Vincetti L., Husakou A., Fourcade-Dutin C., Hoenninger C., Mottay E., Gérôme F., Benabid F. *Opt. Express*, **22**, 10735 (2014).
3. Jaworski P., Yu F., Carter R.M., Knight J.C., Shephard J.D., Hand D.P. *Opt. Express*, **23**, 8498 (2015).
4. Travers J.C., Chang W., Nold J., Joly N.Y., Russell P.St.J. *J. Opt. Soc. Am. B*, **28**, A11 (2011).
5. Belli F., Abdolvand A., Chang W., Travers J.C., Russell P.St.J. *Optica*, **2**, 292 (2015).
6. Couny F., Benabid F., Roberts P.J., Light P.S., Raymer M.G. *Science*, **318**, 1118 (2007).
7. Wang Y.Y., Couny F., Light P.S., Mangan B.J., Benabid F. *Opt. Lett.*, **35**, 1127 (2010).
8. Tani F., Belli F., Abdolvand A., Travers J.C., Russell P.St.J. *Opt. Lett.*, **40**, 1026 (2015).
9. Benoît A., Beaudou B., Alharbi M., Debord B., Gérôme F., Salin F., Benabid F. *Opt. Express.*, **23**, 14002 (2015).
10. Pryamikov A.D., Biriukov A.S., Kosolapov A.F., Plotnichenko V.G., Semjonov S.L., Dianov E.M. *Opt. Express*, **19**, 1441 (2011).
11. Kolyadin A.N., Kosolapov A.F., Pryamikov A.D., Biriukov A.S., Plotnichenko V.G., Dianov E.M. *Opt. Express*, **21**, 9514 (2013).
12. Alagashev G.K., Pryamikov A.D., Kosolapov A.F., Kolyadin A.N., Lukovkin A.Yu., Biriukov A.S. *Laser Phys.*, **25**, 055101 (2015).
13. Belardi W., Knight J.C. *Opt. Express*, **22**, 10091 (2014).
14. Poletti F. *Opt. Express*, **22**, 23807 (2014).
15. Yatsenko Yu.P., Krylov A.A., Pryamikov A.D., Kosolapov A.F., Kolyadin A.N., Gladyshev A.V., Bufetov I.A. *Quantum Electron.*, **46**, 617 (2016) [*Kvantovaya Elektron.*, **46**, 617 (2016)].
16. Pryamikov A.D., Kosolapov A.F., Alagashev G.K., Kolyadin A.N., Velmiskin V.V., Biriukov A.S., Bufetov I.A. *Quantum Electron.*, **46**, 1129 (2016) [*Kvantovaya Elektron.*, **46**, 1129 (2016)].
17. Pryamikov A.D., Alagashev G.K., Kosolapov A.F., Biriukov A.S. *Laser Phys.*, **26**, 125104 (2016).
18. Debord B., Amsanpally A., Chafer M., Baz A., Maurel M., Blondy G.M., Hugonnot E., Scol F., Vincetti L., Gerome F., Benabid F. *Optica*, **4**, 209 (2017).
19. Litchinitser N.M., Abeeluck A.K., Headley C., Eggleton B. *J. Opt. Lett.*, **27**, 1592 (2002).
20. Tani F., Travers J.C., Russell P.St.J. *J. Opt. Soc. Am. B*, **31**, 311 (2014).
21. Dudley J., Taylor R. *Supercontinuum Generation in Optical Fibers* (Cambridge: University Press, 2010).
22. Nibbering E.T.J., Grillon G., Franco M.A., Prade B.S., Mysyrowicz A. *J. Opt. Soc. Am. B*, **14**, 650 (1997).
23. Sprangle P., Penano J.R., Hafizi B. *Phys. Rev. E*, **66**, 046418 (2002).
24. Penano R., Sprangle P., Serafim P., Hafizi J.B., Tang A. *Phys. Rev. E*, **68**, 056502 (2003).
25. Penano J.R., Sprangle P., Hafizi B., Ting A., Gordon D.F., Kapetanakos C.A. *Phys. Plasmas*, **11**, 2865 (2004).